
Check for updates

reduction reaction (ORR) overpotential, and b is the ORR Tafel slope.

The ORR overpotential is determined by equation for the cell potential V_{cell}

$$V_{cell} = V_{oc} - \eta - R_\Omega j, \tag{3}$$

where V_{oc} is the cell open-circuit voltage and R_Ω is the sum of ohmic resistivities in the cell. A last equation follows from the oxygen transport equation in the GDL and it relates the oxygen concentrations c_1 and c:

$$\frac{c_1}{c_{ref}} = \frac{c}{c_{ref}} - \frac{j}{j_{\lim}}, \tag{4}$$

where

$$j_{\lim} = \frac{4FD_b c_{ref}}{l_b} \tag{5}$$

is the limiting current density due to oxygen transport in the GDL, D_b and l_b are the GDL oxygen diffusivity and thickness, respectively.

Introducing dimensionless variables

$$\tilde{z} = \frac{z}{L}, \quad \tilde{j} = \frac{j}{i_* l_t}, \quad \tilde{J} = \frac{J}{i_* l_t}, \quad \tilde{\eta} = \frac{\eta}{b}, \quad \tilde{c} = \frac{c}{c_{ref}}, \quad \tilde{R}_\Omega = \frac{i_* l_t R_\Omega}{b}, \quad \tilde{V} = \frac{V}{b}, \tag{6}$$

expressing η from Eq. (3) and substituting the result and $\tilde{c}_1$ from Eq. (4) into Eq. (2), we get the following problem for $\tilde{c}$ and $\tilde{j}$:

$$\lambda\tilde{J}\frac{\partial\tilde{c}}{\partial\tilde{z}} = -\tilde{j}, \quad \tilde{c}(0) = 1 \tag{7}$$

$$\tilde{j} = \left(\tilde{c} - \frac{\tilde{j}}{\tilde{j}_{\lim}}\right) K_V \exp(-\tilde{R}_\Omega \tilde{j}), \tag{8}$$

where

$$K_V = \exp(\tilde{V}_{oc} - \tilde{V}_{cell}) \tag{9}$$

is a constant parameter, J is the mean current density in the cell,

$$\lambda = \frac{4FvhC_{ref}}{LJ} \tag{10}$$

is the oxygen stoichiometry of the flow, and L is the channel length.

3. Analytical solutions

To solve the system of Eqs.(7) and (8), we solve Eq. (8) for $\tilde{c}$ and substitute the result into Eq. (7); this leads to a decoupled equation for $\tilde{j}$ [12]:

$$\left(\frac{\lambda\tilde{J}}{\tilde{j}_{\lim}}\right)\frac{\partial\tilde{j}}{\partial\tilde{z}} = -\frac{\tilde{j}}{1 + \frac{\tilde{j}_{\lim}}{K_V}(1 + \tilde{R}_\Omega\tilde{j})\exp(\tilde{R}_\Omega\tilde{j})}, \quad \tilde{j}(0) = \tilde{j}^0. \tag{11}$$

Solution to Eq. (11) must obey to the obvious integral condition

$$\int_0^1 \tilde{j}\, d\tilde{z} = \tilde{J}. \tag{12}$$

A key parameter in Eq. (11) is $\tilde{R}_\Omega\tilde{j} \simeq \tilde{R}_\Omega\tilde{J} = R_\Omega J/b$; for typical PEMFCs, the upper value of this parameter is about 3. Here, we take for the estimate $R_\Omega = 0.1\ \mathrm{cm}^2$, $J = 1\ \mathrm{A\,cm}^{-2}$ and b = 0.03 V. Of practical interest is, thus, to study solutions to Eq. (11) in the range $0 \le \tilde{R}_\Omega\tilde{J} \lesssim 3$.

Setting in Eq. (8) $\tilde{R}_\Omega = 0$, we get

$$\tilde{j} = \alpha\tilde{c}, \tag{13}$$

get $\tilde{c} = \exp(-\alpha\tilde{z}/(\lambda\tilde{J}))$. Substituting this [illegible] into Eq. (12) to eliminate α, we find [8,9]

$$\tilde{j} = -\lambda\ln\left(1 - \frac{1}{\lambda}\right)\tilde{J}\left(1 - \frac{1}{\lambda}\right)^{\tilde{z}} \tag{15}$$

$$\tilde{c} = \left(1 - \frac{1}{\lambda}\right)^{\tilde{z}}. \tag{16}$$

These are the zero-order approximations of $\tilde{j}(\tilde{z})$ and $\tilde{c}(\tilde{z})$, which correspond to vanishingly small product $\tilde{R}_\Omega\tilde{j}$. Note that Eqs.(15) and (16) do not contain K_V and $j_{\lim}$.

Solution for the first-order approximation of a small but non-zero $\tilde{R}_\Omega\tilde{j}$ can be obtained as follows. Expanding the right side of Eq. (11) in Taylor series over small $\tilde{R}_\Omega$ and keeping two leading terms, we get

$$\lambda\tilde{J}\frac{\partial\tilde{j}}{\partial\tilde{z}} = -\alpha\tilde{j} + \frac{2\alpha^2\tilde{R}_\Omega\tilde{j}^2}{K_V}, \quad \tilde{j}(0) = \tilde{j}^0. \tag{17}$$

Eq. (17) is separable and it can easily be integrated. Using Eq. (12) to eliminate $\tilde{j}^0$ from the solution, we get

$$\tilde{j} = \frac{K_V}{2\alpha\tilde{R}_\Omega D}\left(1 - \exp\left(-\frac{2\alpha^2\tilde{R}_\Omega}{\lambda K_V}\right)\right), \tag{18}$$

where

$$D \equiv 1 - \exp\left(-\frac{\alpha(1-\tilde{z})}{\lambda\tilde{J}}\right) + \exp\left(-\frac{2\alpha^2\tilde{R}_\Omega}{\lambda K_V}\right)\left(\exp\left(\frac{\alpha\tilde{z}}{\lambda\tilde{J}}\right) - 1\right). \tag{19}$$

Integrating Eq. (7) with $\tilde{j}$ from Eq. (18), we get the oxygen concentration along the channel:

$$\tilde{c} = 1 - \frac{K_V}{2\alpha^2\tilde{R}_\Omega}\left\{\frac{\alpha\tilde{z}}{\lambda\tilde{J}} + \ln\left(\exp\left(\frac{\alpha}{\lambda\tilde{J}}\right) - 1\right) - \ln\left[\exp\left(\frac{\alpha(K_V - 2\alpha\tilde{R}_\Omega\tilde{J})}{K_V\lambda\tilde{J}}\right)\left(\exp\left(\frac{\alpha\tilde{z}}{\lambda\tilde{J}}\right) - 1\right) - \exp\left(\frac{\alpha\tilde{z}}{\lambda\tilde{J}}\right) + \exp\left(\frac{\alpha}{\lambda\tilde{J}}\right)\right]\right\}. \tag{20}$$

The solutions (18) and (20) work well up to $\tilde{R}_\Omega\tilde{J} \simeq 0.3$ (see below).

The first-order solutions (18) and (20) explicitly depend on $\tilde{j}_{\lim}$ through α and on K_V. The parameter K_V, Eq. (9), exponentially depends on the cell open-circuit voltage, which is usually unknown. Moreover, measuring a true V_{oc} is a difficult task, as at zero current in the external load, the cell supports a non-zero internal current due to hydrogen crossover through the membrane. Typically, crossover lowers the theoretical V_{oc} by 100 to 200 mV.

However, if the cell polarization curve is available, parameter K_V can be found from the zero-order solutions. We take a small cell current $\tilde{J}^*$, so that $\tilde{R}_\Omega\tilde{J}^*$ and $\tilde{J}^*/\tilde{j}_{\lim}$ are vanishingly small. In that case, Eq. (8) simplifies to $\tilde{j} = K_V^*\tilde{c}$. Comparing this to the zero-order solutions, Eqs. (15) and (16), we see that

$$K_V^* = -\lambda\ln\left(1 - \frac{1}{\lambda}\right)\tilde{J}^*. \tag{21}$$

With Eq. (9), we find the true open-circuit voltage:

$$\tilde{V}_{oc} = \ln(K_V^*) + \tilde{V}_{cell}^*, \tag{22}$$

where $\tilde{V}_{cell}^*$ corresponds to $\tilde{J}^*$. Once $\tilde{V}_{oc}$ is determined, parameter K_V for lower cell potentials can be found from Eq. (9). This procedure requires knowledge of a single low-current point (J^*, V_{cell}^*) on the cell polarization curve.

one is a boundary

Basically, there are two problem formulations for Eq. (11). From Eq. (10), it is seen that the product $\lambda\tilde{J}$ on the left side of Eq. (11) is independent of $\tilde{J}$. Thus, the first option is to fix an arbitrary $\tilde{j}^0$, solve numerically Eq. (11), and to calculate the respective mean current density $\tilde{J}$ from Eq. (12). This approach has been taken by Chevalier et al. [12] for equation analysis and illustration purposes.

In practice, the cell polarization curve is usually available from experiments, which means that one is interested in the shape of local current corresponding to a certain pair ($\tilde{J}$, $\tilde{V}_{cell}$). In this case, $\tilde{J}$ is given and $\tilde{j}^0$ has to be found from Eq. (12). A possible way to solve the system Eqs. (11) and (12) in this case is as follows. We formulate the problem as a least-squares one, i.e., starting from some initial $\tilde{j}^0$, we seek for $\tilde{j}^0$ which minimizes the merit function

$$\left(\int_0^1 \tilde{j}\,(\tilde{z};\tilde{j}^0)d\tilde{z} - \tilde{J}\right)^2 \to \min. \tag{23}$$

A good starting point is $\tilde{j}^0 = \tilde{J}$. To minimize the function Eq. (23), we used the *leastsq* routine from the Python Scipy library. This routine employs the Levenberg-Marquardt algorithm of optimization; for the problem Eqs. (11) and (23), the algorithm is stable and robust. A Python code for the problem solution can be downloaded from https://github.com/akulikovsky/Local-current/blob/master/Local_current_solver.py.

5. Experimental

Local current density measurements have been performed using a segmented cell system and a test station developed at Hawaii Natural Energy Institute [13]. The segmented cell setup consists of the cell hardware, the custom designed current transducer system, the data acquisition device and a single cell test station. HNEI's system has closed loop Hall sensors (Honeywell CSNN 191) for current detection and an improved data acquisition system, which allows us the simultaneous data collection from 10 current channels. The segmented cell system is typically operated as a single cell using the test station and standard testing protocols which simulates real conditions since only an overall cell load is controlled.

The segmented cell hardware is based on 100 cm^2 cell and consists of non-segmented and segmented flow field plates and GDLs. Both the plates have the same ten parallel channel serpentine design arranged in co-flow configuration. The segmented plate consists of 10 segments with an area of 7.6 cm^2; the segments are arranged in two parallel rows. Inlet is at segment 1 and the outlet at segment 10. Each segment has its own current collector and GDL. The segmentation was applied to the cathode.

Catalyst coated membranes (CCM) from Gore with the active area of 100 cm^2 have been used. Catalyst loading was 0.4 $mg_{Pt}\,cm^{-2}$ for anode and cathode with the catalyst layer thickness of 10–12 μ m. The thickness of reinforced membrane varied in the range of 16–18 μ m. Sigracet 25BC was used as GDLs for both the electrodes. 25BC consists of carbon paper and microporous layer with the total thickness of 220–235 μ m and porosity of 80%. Teflon gaskets (125 μ m) were employed for both electrodes to ensure a required compression ratio.

The cell was operated with H_2 /air gas configuration at a cell temperature of 80 °C. The anode/cathode conditions were 2/2 stoichiometry, 100/50% relative humidity and 150/150 kPa backpressure.

6. Results and discussion

The true V_{oc} of our cell has been estimated from Eq. (22) using the

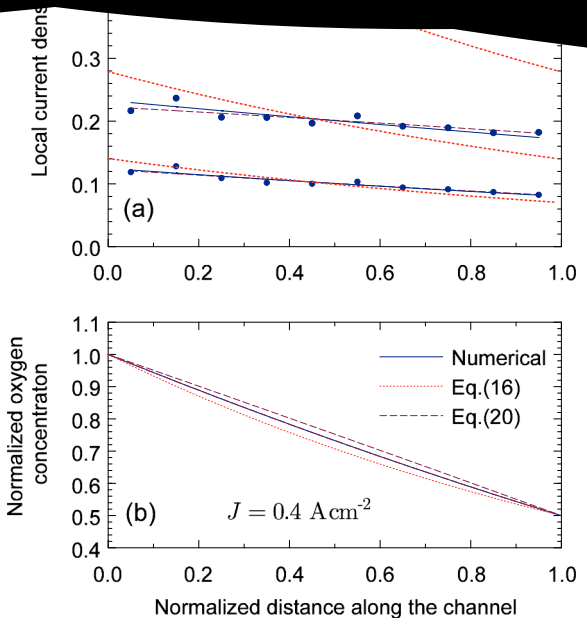

Fig. 1. (a) Experimental (points) and numerical solution to (11), (12) (solid lines) shapes of the local current density along the air channel. For comparison, the shapes corresponding to zero ohmic resistance (Eq. (15), dotted lines), and for the case of a small parameter $\tilde{R}_\Omega\tilde{J}$ (Eq. (18), dashed lines) are shown. (b) Numerical (solid line) and analytical, (dashed and dotted lines) normalized oxygen concentration c/c_{ref} along the channel.

data for the smallest $J^* = 101.28\,mA\,cm^{-2}$ (see the code). It gives $V_{oc} = 1.1688$ V; however, a more accurate results are obtained with slightly lower $V_{oc} = 1.1649$ V. The last value of V_{oc} has been fixed in the calculations.

The experimental and model shapes of the local current density j are shown in Fig. 1a for the mean cell currents of 100, 200 and 400 $mA\,cm^{-2}$. Parameters for the calculations are listed in Table 1. As can be seen, the agreement between the experiment and numerical model is very good. For comparison, the zero-order shapes Eq. (15) and the first-order shapes, Eq. (18), are also shown. As can be seen, for our set of the cell parameters, Eq. (15) well describes $j(z)$ for J below 100 $mA\,cm^{-2}$; for larger currents, the zero-order approximation fails. The first-order Eq. (18) works very well for J = 100 and 200 $mA\,cm^{-2}$ (Fig. 1a). However, for J = 400 $mA\,cm^{-2}$, Eq. (18) gives a wrong slope

Table 1
Geometrical and operating parameters of the cell. Parameters of the experimental cell polarization curve are listed in the Python code. R_Ω was measured by impedance spectroscopy.

Catalyst layer thickness l_t, μm	12
Gas diffusion layer thickness l_b, μm	235
Channel depth h, cm	0.15
Channel length L, cm	52.78
ORR Tafel slope b, V	0.03
ORR exchange current density i_*, A cm^{-3} (assumed)	10^{-3}
GDL oxygen diffusivity D_b, $cm^2\,s^{-1}$	0.02
Cell ohmic resistivity R_Ω, Ω cm^2	0.045
Cathode flow stoichiometry λ	2
Cathode flow relative humidity	50%
Absolute pressure, kPa	150
Cell temperature, K	273 + 80

the local current [illegible]

The results show that the quasi-2d, along-the-channel model, Eqs. (11) and (12), well describes the experimental shape of the local current density in our 2d segmented cell. The reason is, perhaps, small variation of the local current over the cell surface (Fig. 1a), which means that true 2d effects due to spatial variation of η are small. Another effect that potentially could affect the 1D distribution of $j(z)$ is under-rib oxygen transport between two adjacent turns of the meander channel [14]. Fig. 1a suggest that in our cell, this effect is not large. Note that R_Ω was assumed to be independent of z, i.e., the model does not describe situations with local membrane drying. The model is based of the Tafel equation for the local j. This approximation holds if j is less than (strictly speaking, much less than) the characteristic current densities for the proton $j_p = \sigma_p b/l_t$ and oxygen $j_{ox} = 4FD_{ox}c_{ref}/l_t$ transport in the CCL. Here, σ_p is the CCL proton conductivity and D_{ox} is the CCL oxygen diffusivity. Using the approximations for $\sigma_p(J)$, $D_{ox}(J)$ and $b(J)$ obtained for a modern Pt/C electrode from Gore [15], it can be shown that the relation $1.8\,J < \min\{j_p, j_{ox}\}$ holds for J below 0.4 A cm^{-2}. Further, with the data [14], at $J = 0.4$ A cm^{-2}, the resistivity due to oxygen transport loss in the CCL $R_{ox} \simeq bl_t/(12FD_{ox}c_{ref}) \simeq 0.036\ \Omega\ \text{cm}^2$ and the resistivity due to proton transport in the CCL $R_p \simeq l_t/(3\sigma_p) \simeq 0.007\ \Omega\ \text{cm}^2$. We see that $R_p \ll R_\Omega$, while $R_{ox} \simeq R_\Omega$. The reason why R_{ox} does not affect the model shapes in Fig. 1a is not clear yet; understanding this effect requires incorporation of oxygen transport in the CCL into the model. It is interesting to note that oxygen transport in the GDL does not affect the zero-order shapes of Eq. (15).

The model ignores the gradient of oxygen concentration across the channel. CFD calculations show that this gradient is small, e.g., in Fig. 8 of Ref. [16], at the current density of 300 mA cm^{-2}, variation of c across the channel is less than 0.5%. Analytical model [10] also shows that below 1 A cm^{-2}, the effect of oxygen diffusion across the channel is marginal.

Last but not least, it should be emphasized that non-zero ohmic resistivity of the cell homogenizes local current distribution, which otherwise would have been strongly nonuniform (cf. dotted and solid curves for $J = 400$ mA cm^{-2} in Fig. 1a). As a major contribution to R_Ω gives the membrane, this result emphasizes again the importance of water management and selection of proper membrane thickness in PEMFCs.

7. Conclusions

Analysis of a recent model [12] for the distribution of local current density $j(z)$ along the cathode channel of a PEM fuel cell is performed. Analytical solution for $j(z)$ is obtained in the limit of small cell ohmic resistivity R_Ω. For arbitrary R_Ω, an algorithm for numerical solution of

Comparison of solutions [illegible]

homogenizes the shape of $j(z)$.

Acknowledgments

T. Reshetenko gratefully acknowledges funding from US Office of Naval Research (N00014-15-1-0028) and US Army Research Office (W911NF-15-1-0188). The authors are thankful to Günter Randolf and Jack Huizingh for valuable help in the system operation and the Hawaiian Electric Company for ongoing support of the Hawaii Sustainable Energy Research Facility.

References

[1] S.J.C. Cleghorn, C.R. Derouin, M.S. Wilson, S. Gottesfeld, A printed circuit board approach to measuring current distribution in a fuel cell, J. Appl. Electrochem. 28 (1998) 663–672.
[2] J. Stumper, S.A. Campbell, D.P. Wilkinson, M.C. Johnson, M. Davis, In–situ methods for the determination of current distributions in PEM fuel cells, Electrochim. Acta 43 (1998) 3773–3783.
[3] D.J.L. Brett, S. Atkins, N.P. Brandon, V. Vesovic, N. Vasileadis, A. Kucernak, Localized impedance measurements along a single channel of a solid polymer fuel cell, Electrochem. Solid-State Lett. 6 (2003) A63–A66.
[4] I.A. Schneider, H. Kuhn, A. Wokaun, G.G. Scherer, Fast locally resolved electrochemical impedance spectroscopy in polymer electrolyte fuel cells, J. Electrochem. Soc. 152 (2005) A2092–A2103.
[5] T.V. Reshetenko, G. Bender, K. Bethune, R. Rocheleau, A segmented cell approach for studying the effects of serpentine flow field parameters on PEMFC current distribution, Electrochim. Acta 88 (2013) 571–579.
[6] N. Zamel, A. Bhattarai, D. Gerteisen, Measurement of spatially resolved impedance spectroscopy with local perturbation, Fuel Cells 13 (2013) 910–916.
[7] M.A. Khan, B. Sundn, J. Yuan, Analysis of multi-phase transport phenomena with catalyst reactions in polymer electrolyte membrane fuel cells? A review, J. Power Sources 196 (2011) 7899–7916.
[8] A.A. Kulikovsky, The effect of stoichiometric ratio λ on the performance of a polymer electrolyte fuel cell, Electrochim. Acta 49 (2004) 617–625.
[9] A.A. Kulikovsky, A. Kuèernak, A. Kornyshev, Feeding PEM fuel cells, Electrochim. Acta 50 (2005) 1323–1333.
[10] A.U. Thosar, A.K. Lele, Analytical solutions of an isothermal two-dimensional model of a cathode flow channel in a proton exchange membrane fuel cell, Chem. Eng. Sci. 190 (2018) 333–344.
[11] J.X. Liu, H. Guo, F. Ye, C.F. Ma, Two-dimensional analytical model of a proton exchange membrane fuel cell, Energy 119 (2017) 299–308.
[12] S. Chevalier, C. Josset, B. Auvity, Analytical solutions and dimensional analysis of pseudo 2D current density distribution model in PEM fuel cells, Renew. Energy 125 (2018) 738–746.
[13] T. Reshetenko, A. Kulikovsky, PEM fuel cell characterization by means of the physical model for impedance spectra, J. Electrochem. Soc. 162 (2015) F627–F633.
[14] J.G. Pharoah, On the permeability of gas diffusion media used in PEM fuel cells, J. Power. Sources 144 (2005) 77–82.
[15] T. Reshetenko, A. Kulikovsky, Variation of PEM fuel cell physical parameters with current: impedance spectroscopy study, J. Electrochem. Soc. 163 (2016) F1100–F1106.
[16] V. Gurau, H. Liu, S. Kakac, Two-dimensional model for proton exchange membrane fuel cells, AIChE J. 44 (1998) 2410–2422.